1

2

3

Simulating precipitation radar observations from a geostationary satellite

By

Atsushi Okazaki[1], Takumi Honda[1], Shunji Kotsuki[1,2],
Moeka Yamaji[3], Takuji Kubota[3], Riko Oki[3],
Toshio Iguchi[4],
and Takemasa Miyoshi[1,2,5,6,7]

[1]RIKEN Center for Computational Science, Kobe, Japan
[2] RIKEN interdisciplinary Theoretical and Mathematical Sciences Program, Kobe, Japan
[3]Earth Observation Research Center, Japan Aerospace Exploration Agency, Tsukuba, Japan
[4]National Institute of Information and Communications Technology, Koganei, Japan
[5]Department of Atmospheric and Oceanic Science, University of Maryland, College Park, College Park, Maryland
[6]Japan Agency for Marine-Earth Science and Technology, Yokohama, Japan
[7]Prediction Science Laboratory, RIKEN Cluster for Pioneering Research, Kobe, Japan

Corresponding authors: Atsushi Okazaki and Takemasa Miyoshi, RIKEN Center for Computational Science, 7-1-26 Minatojima-minami-machi, Chuo-ku, Kobe, Hyogo 650-0047, Japan (atsushi.okazaki@riken.jp, takemasa.miyoshi@riken.jp)

1

Abstract

Spaceborne precipitation radars, such as the Tropical Rainfall Measuring Mission (TRMM) and the Global Precipitation Measurement (GPM) Core Observatory, have been important platforms to provide a direct measurement of three-dimensional precipitation structure globally. Building upon the success of TRMM and GPM Core Observatory, the Japan Aerospace Exploration Agency (JAXA) is currently surveying the feasibility of a potential satellite mission equipped with a precipitation radar on a geostationary orbit. The quasi-continuous observation realized by the geostationary satellite radar would offer a new insight into meteorology and would advance numerical weather prediction (NWP) through their effective use by data assimilation.

Although the radar would be beneficial, the radar on the geostationary orbit measures precipitation obliquely at off-nadir points. Besides, the observing resolution will be several times larger than those onboard TRMM and GPM Core Observatory due to the limited antenna size that we could deliver. The tilted sampling volume and the coarse resolution would result in more contamination from surface clutter. To investigate the impact of these limitations and to explore the potential usefulness of the geostationary satellite radar, this study simulates the observation data for a typhoon case using an NWP model and a radar simulator.

The results demonstrate that it would be possible to obtain three-dimensional precipitation data. However, the quality of the observation depends on the beam width, the beam sampling span, and the position of precipitation systems. With a wide beam width and a coarse beam span, the radar cannot observe weak precipitation at low altitudes due to surface clutter. The limitation can be mitigated by oversampling (i.e., a wide beam width and a fine sampling span). With a narrow beam width and a fine beam sampling span, the surface clutter interference is confined to the surface level. When the precipitation system is located far from the nadir, the precipitation signal is obtained only for strong precipitation.

1. Introduction

Knowing the distribution of precipitation in space and time is essential for scientific developments as precipitation plays a key role in global water and energy cycles in the Earth system. Such knowledge is also indispensable to our daily lives and disaster monitoring and prevention. However, observing precipitation globally is not an easy task. Ground-based observations may not adequately represent the rainfall amounts of a broader area since the vast surface of the earth remains unobserved (Kidd et al., 2016). Alternatively, satellites provide an ideal platform to observe precipitation globally. There are three types of methods to observe or estimate precipitation from satellites: visible and infrared, passive microwave, and active microwave (radar). Among them, radar is the most direct method and is the only sensor that can provide three-dimensional structure of precipitation. The first satellite equipped with precipitation radar was the Tropical Rainfall Measuring Mission (TRMM) launched in 1997 (Kummerow et al., 1998; Kozu et al., 2001), and the first satellite-borne dual-frequency precipitation radar onboard the Global Precipitation Measurement (GPM) Core Observatory was launched in 2014 (Hou et al., 2014; Skofronick-Jackson et al., 2017). The observations produced by the precipitation radars onboard the low-earth-orbiting satellites have been contributing to enhance our knowledge on meteorology. For instance, their ability to see through clouds helps understand storm structures (Kelly et al., 2004) and the nature of convection (e.g. Takayabu 2006; Hamada et al., 2015; Houze et al., 2015).

Building upon the success of the TRMM and GPM Core Observatory, the Japan Aerospace Exploration Agency (JAXA) is currently studying the feasibility of a geostationary satellite equipped with precipitation radar (hereafter, simply "GPR"). The main advantage of GPR over the existing ones with precipitation radar is the observation frequency. Because the previous satellites are low earth orbiters, they cannot observe the same area frequently. For instance, TRMM overpasses a 500 by 500 km^2 box 1-2 times a day on average (Bell et al., 1990). To make the situation worse, it is difficult to capture the whole figure of a large-scale precipitation system (e.g. tropical cyclone) at once due to the

narrow scan swath (e.g. 245 km for KuPR on GPM Core Observatory). Alternatively, GPR stays at the same location all the time and continuously measures precipitation in its range of observation. Those data are expected to help understand important scientific issues. Furthermore, those frequent data could improve the skill of numerical weather prediction (NWP) through data assimilation, leading to more accurate and timely warnings of floods and landslides.

Although GPR would be beneficial, it has potential disadvantages. Since GPR measures precipitation from the geostationary orbit, it measures precipitation obliquely at off-nadir points. It is unclear how severely this may degrade the observation. In addition, the tilted sampling volume worsens the contamination of the precipitation echo by the surface clutter. Takahashi (2017) showed that the clutter height monotonically increases with the incidence angle from the wide swath observation during the end-of-mission experiment of the TRMM. The impact of the surface clutter interference with a large incidence angle would be large if the horizontal resolution of the radar is coarse, and that is the case for GPR. The horizontal resolution is limited by the antenna size and wavelength. A larger antenna is needed for higher resolution. However, it is challenging to construct a large antenna on a geostationary orbit. The JAXA has launched a satellite with a relatively large antenna of 19 m by 17 m (ETS-VIII, Meguro et al., 2009). Based on the experience and further efforts (Joudoi et al, 2018), currently we consider a 30-m-by-30-m square antenna as a feasible choice, whose spatial resolution is 20 km at nadir, that is several times larger than that of TRMM/PR (4.3 km). To investigate the mission feasibility of GPR, it is important to simulate observation of GPR and to find its potential usefulness and weakness.

In the past decade, a geostationary radar instrument known as the Next Generation Weather Radar (NEXRAD) In Space (NIS; Im et al., 2007) has been proposed. A few studies demonstrated the capability of NIS. Lewis et al. (2011) examined the feasibility of a 35 GHz Doppler radar to observe the wind field. They showed that the direct measurement of winds from the geostationary orbit would be possible for a hurricane case. Li et al. (2017) evaluated the impact of surface clutter for the same

radar assuming a uniform rain layer. They showed that most of rain echoes at off-nadir scanning angles will not be contaminated by the surface clutter, when rain intensity is greater than 10 mm h^{-1}.

However, the impact of the surface clutter and the oblique measurement would depend on the shape and position of the precipitation system. This study extends Li et al. (2017) for a realistic case. By considering the importance to societal and scientific benefit, we chose a typhoon as a test case in this study. We investigate the impact with various typhoon locations and radar parameters such as radar beam width and sampling span for realistic scenarios of a simulated typhoon case.

This paper is structured as follows. Section 2 describes the proposed specifications of GPR and presents the newly-developed radar simulator. Section 3 describes the characteristics of the observation with GPR for an idealized case. Section 4 presents the results of applying the radar to a typhoon case. Section 5 provides the sensitivity results to the location of the typhoon. Section 6 shows the impact of attenuation and sidelobe clutter. Finally, Section 6 provides conclusions.

2. Radar simulator

2.1. Radar specifications

The specifications of GPR are summarized in Table. 1. The GPR is anticipated at 13.6 GHz, the same as KuPR onboard GPM Core Observatory. We assume a 30-m-by-30-m square phased array radar with the half-power beam width (-3 dB) of 0.032°, with which we can achieve horizontal resolution of 20 km at the nadir point on the earth surface. The range resolution is 500 m. Though shorter-range resolution is technically viable, we adopt this value by considering the balance to the horizontal resolution. The number of the range bins is 60; the corresponding height of the beam center ranges from the surface to 30 km at nadir. The scan angle is ±6°, which covers a circular disk with a diameter of 8400 km on Earth's surface. If GPR were placed at 135°E of the equator, it would cover from Sumatra to New Caledonia, and from Australia to the southern half of Japan.

We assume that the satellite can complete the full disk scan within one hour. In addition to the normal

132 mode, it is expected to have several modes and can observe a targeting precipitation system intensively

133 as in Himawari-8 (Bessho et al., 2016). In this study, we focus only on snap-shots and do not consider

134 the time for GPR to complete the full disk scan.

135

2.2. Precipitation reflectivity

137   This subsection describes how to calculate reflectivity measured by GPR (Z). First, we convert

138 model hydrometeors (cloud water, cloud ice, rain, snow, and graupel) to total backscattering ($\overline{\sigma}_b$) and

139 extinction coefficients ($\overline{k}_{ext}$) at every model grid point using an existing software called Joint

140 Simulator for Satellite Sensors (Joint-Simulator; Hashino et al., 2013). The Joint-Simulator is a suite

141 of software that simulates satellite observations based on atmospheric states simulated by cloud-

142 resolving models. The total backscattering and extinction coefficients are obtained respectively by

143 summing single-particle backscattering (σ_b^s) and extinction coefficients (k_{ext}^s) for the i th hydrometeor

144 specie following its drop size (D) distribution ($N(D)$) as follows:

$$\overline{\sigma}_b = \sum_{i=1}^{n_{spec}} \int_0^{\infty} \sigma_{b,i}^s(D)N(D)dD, \tag{1}$$

$$\overline{k}_{ext} = \sum_{i=1}^{n_{spec}} \int_0^{\infty} k_{ext,i}^s(D)N(D)dD, \tag{2}$$

145 where n_{spec} is the number of the hydrometeor species. In this study, up to five hydrometeor species,

146 i.e., cloud water, cloud ice, rain, snow, and graupel, were considered. The Mie approximation is used

147 to calculate $\sigma_{b,i}^s$ and $k_{ext,i}^s$ for all the species (Masunaga and Kummerow, 2005). After calculating

148 $\overline{\sigma}_b$ and $\overline{k}_{ext}$ at every model grid point, the grid point values are integrated over the scattering volume

149 following the antenna pattern. The radar-received power from precipitation (P_r) of the beam pointing

150 range r_0 and scan angle θ_0 and ϕ_0 is given by

$$P_r$$
$$= \frac{P_t \lambda^2}{(4\pi)^3} \int_{r_0-c\tau/4}^{r_0+c\tau/4} \int_{\theta_0-\pi}^{\theta_0+\pi} \int_{\phi_0-\pi/2}^{\phi_0+\pi/2} f^4(\theta,\phi)\overline{\sigma}_b(r,\theta,\phi)A_P(r,\theta,\phi)\, r^{-2}\, cos\theta\, d\phi\, d\theta\, dr, \tag{3}$$

151   where P_t is the transmitted power, c the speed of light, τ the pulse duration, and f^4 the two-way

152   effective beam weighting function. We assumed the uniform antenna pattern, whose sidelobe level is

153   -13.26 dB:

$$f^2(\psi) = \left(\frac{\sin\psi}{\psi}\right)^2 \tag{4}$$

154   where $\psi = \sqrt{(\theta - \theta_0)^2 + (\phi - \phi_0)^2}/\Psi$, Ψ is obtained by solving the equation $f^2\left(\frac{\theta_B}{2}/\Psi\right) = 0.5$,

155   and θ_B is the half-power beam width (-3 dB). $A_P(r, \theta, \phi)$ is the attenuation factor from the radar to

156   range r in the direction of (θ, ϕ) and calculated by

$$A_P(r, \theta, \phi) = \exp\left[-0.2\ln(10)\int_0^r \bar{k}_{ext}(r', \theta, \phi)dr'\right]. \tag{5}$$

157   The radar reflectivity measured by GPR is calculated as follows:

$$Z = \frac{\lambda^4}{\pi^5|K|^2}\frac{\int_{r_0-\frac{c\tau}{4}}^{r_0+\frac{c\tau}{4}}\int_{\theta_0-\pi}^{\theta_0+\pi}\int_{\phi_0-\frac{\pi}{2}}^{\phi_0+\frac{\pi}{2}}f^4(\theta, \phi)\bar{\sigma}_b(r, \theta, \phi)A_P(r, \theta, \phi)\cos\theta \, d\phi \, d\theta \, dr}{\int_{r_0-\frac{c\tau}{4}}^{r_0+\frac{c\tau}{4}}\int_{\theta_0-\pi}^{\theta_0+\pi}\int_{\phi_0-\frac{\pi}{2}}^{\phi_0+\frac{\pi}{2}}f^4(\theta, \phi)r^{-2}\cos\theta \, d\phi \, d\theta \, dr}, \tag{6}$$

158   where λ is the wavelength, K the function of a complex refractivity index of scattering particles.

159   Following Masunaga and Kummerow (2005), $|K|^2$ is assumed to be a constant (0.925) in this study.

160   We do not consider the impact of attenuation ($A_P = 1.0$ everywhere) as it can be corrected with proper

161   methods (e.g. Iguchi et al., 2000) for Sects. 3, 4, and 5.

162

163   **2.3. Surface clutter**

164   Surface clutter echoes contaminate the precipitation signals. In this study, we assumed that the

165   surface is completely covered by the ocean for simplicity. Radar-received power from the sea surface

166   (P_s) was calculated by

$$P_s = \frac{P_t\lambda^2}{(4\pi)^3}\iint_S \frac{f^4(\theta, \phi)\sigma_0 A_P(r, \theta, \phi)}{r^4}dS \tag{7}$$

167   where σ_0 is the normalized radar cross section (NRCS) of the ocean surface, and S the scattering

168   area. We obtained σ_0 using a model proposed by Wentz et al. (1984) based on observations from a

169   microwave scatterometer onboard the Seasat satellite. The model expresses σ_0 as,

$$\sigma_0 = b_0 (U_{10})^{b_1} \tag{8}$$

170   where U_{10} is the 10-m wind speed, and b_0 and b_1 are fitted parameters. The NRCS for various wind

171   speed is shown in Fig. 2. When raindrops hit the ocean surface, they change the properties of the

172   surface and the scattering signals (Bliven et al., 1997). The impact of impinging rain is negligible at

173   high wind speed (e.g. Braun et al., 1999; Contreras et al., 2003). Since this study focuses on a typhoon

174   case accompanying strong winds, we do not consider the impact of impinging rain. Also, we do not

175   consider the impact of sidelobe clutter as it can be filtered with proper methods (e.g. Kubota et al.,

176   2016) for Sects. 3, 4, and 5.

177

178   **3.   Homogeneous case**

179   To understand the characteristics of the radar observation, we first show the results from an idealized

180   case, in which we assume the atmosphere below 2 km is uniformly filled with a certain amount of

181   hydrometeor. We tested five cases: 20, 30, 40, 50, and 60 dBZ. The corresponding precipitation

182   intensity is roughly 1, 2, 5, 20, and 60 mm h^{-1} if the hydrometeor consists of only rain. The 10-m wind

183   speed was fixed at 10 m s^{-1} uniformly for all cases. The horizontal resolution of the radar was assumed

184   to be 20 km at the nadir point.

185   Figure 3a shows P_r for the case of 60 dBZ. Two features are apparent in the figure. The first is that

186   the precipitation signal is beyond the precipitation area and becomes taller along with the distance

187   from the nadir, and the second is that P_r decreases monotonically with height. Here and hereafter, the

188   distance was measured along the earth surface.

189   Before discussing the reason for these, first we explain the scattering volume of the GPR. Here, the

190   scattering volume of the beam pointing range r_0 and scan angle θ_0 and ϕ_0 is defined as the area

191   where r, θ, and ϕ satisfy both $r_0 - \frac{c\tau}{4} \le r \le r_0 + \frac{c\tau}{4}$ and ψ less than the first null point (Fig. 1).

192   Note that sidelobe area is not included in the scattering volume in this section. Figure 4 shows a

193   schematic of the scattering volume. At the nadir, the incidence angle is zero, and the scattering volume

194   is nearly parallel to the earth surface (Fig. 4a). As the incidence angle increases, the scattering volume

195   becomes tilted against the earth surface (Fig. 4b). As a result, the upper edge of the scattering volume

196   reaches as high as 16 km when the beam center of the GPR is at a point 4000 km away from the nadir

197   even in the lowest range bin (range bin number 1 in Fig. 5b). In the same angle but the highest range

198   bin, the scattering volume ranges from 4 km to 38 km in height (range bin number 60 in Fig. 5b). The

199   range of the scattering volume is even larger with sidelobe area.

200   When the beam center is at the level higher than the precipitating area, there is no precipitation

201   around the beam center. On the other hand, the tip of the scattering volume may touch the precipitating

202   area with the tilted scattering volume at off-nadir. In such a case, the scattering volume is not fully

203   filled with precipitation. Such nonuniform beam filling (NUBF) results in the reduction of P_r with

204   $\overline{\sigma}_b = 0$ in the upper part of the volume compared with the fully filled case. Although the value is small,

205   still GPR catches the signal of precipitation, and thus P_r has a value even when the beam center is at

206   the point higher than the precipitating area. As the scattering volume becomes more tilted against the

207   earth surface along with the distance from the nadir (Fig. 5a), the maximum height at which the beam

208   gets a signal from precipitation becomes higher along with the distance from the nadir. Hence, we have

209   the signal beyond the precipitation area and the area becomes taller along with the distance from the

210   nadir.

211   The P_r magnitude dependence on the height is also explained by the NUBF. Due to the

212   experimental setting where precipitation exists only in the atmosphere below 2 km, the beam with the

213   scattering volume touching the level higher than 2 km is not fully filled with precipitation. The higher

214   the GPR observes, the less the scattering volume is filled with precipitation. Accordingly, P_r

215   decreases with height.

216   The pattern of P_s is similar to that of P_r, showing dependence on the distance from the nadir (Fig.

217   3b) because σ_0 is a function of the incidence angle (Fig. 2).

9

218   Figure 6 shows signal-to-clutter ratio (SCR) defined as P_r/P_s (dB). The larger SCR, the less

219   contaminated by the clutter. In the figure, areas where the reflectivity from precipitation exceeds 0

220   dBZ are shaded. For all the cases, SCR is the largest at nadir and high altitudes. The minimum SCR is

221   found at the surface level around 500 km away from the nadir reflecting the peak of the echo from the

222   surface clutter. As expected, SCR becomes large when precipitation is strong since the received power

223   from the precipitation becomes larger while P_s is the same for all the cases. The GPR can perceive

224   precipitation only at the nadir point and high altitudes in the case of 20 dBZ (Fig. 6a), but SCR is larger

225   than zero over the whole precipitating area in the case of 60 dBZ (Fig. 6e) except for the surface level

226   in 0 to 1000 km away from the nadir. The comparison of the two cases also suggests that the surface

227   clutter contaminates the precipitation signal from high altitudes for weak precipitation. On the other

228   hand, if the precipitation is strong enough, the clutter interference is limited, and we should get the

229   signal even at the surface level.

230   The simulated results are consistent with Takahashi (2017) and Li et al. (2017), suggesting that both

231   results be plausible.

232

233   **4. Typhoon case**

234   Section 3 presented the characteristics of reflectivity of GPR. However, what we can observe will

235   depend on the size and structure of the target precipitation system. To investigate the capability of GPR

236   in detail, we ran an atmospheric model and applied the radar simulator to produce synthetic

237   observations of reflectivity. As an example, we chose Typhoon Soudelor in 2015, which was the

238   strongest typhoon in that year. Soudelor, generated on 1 August 2015 around the Marshall Islands,

239   rapidly intensified to Super Typhoon equivalent to Category 5 Hurricane within 24 hours from

240   generation and dissipated on 11 August 2015. In this study, we focused on the mature stage of Soudelor

241   at 0000 UTC 5 August 2015.

242   In this section, we focus on the sensitivity to two radar parameters: beam width and beam sampling

span. Three cases were examined: the first adopts the beam width and sampling span of 20 km, the experiment named "bw20bs20". The second uses 20-km resolution of beam width, but the beam span is chosen to be 5 km (bw20bs05), representing an over-sampling case. The third uses the 5-km beam width and span (bw05bs05). Although it is unrealistic to assume a radar with the 5-km beam width at this moment, exploring what kind of observations we can get with the 5-km beam width would be beneficial for the antenna design in the future. The radar settings are summarized in Table 2.

4.1. SCALE-RM simulation

We used a regional cloud-resolving model, SCALE-RM version 5.0.0 (Nishizawa et al., 2015; Sato et al., 2015) to simulate Soudelor. SCALE-RM is based on the SCALE library for weather and climate simulations. The source code and documents of the SCALE library including SCALE-RM are publicly available at http://r-ccs-climate.riken.jp/scale/. The moist physical process is parameterized by a 6-class single-moment bulk microphysics scheme (Tomita et al., 2008), and the five species of hydrometeors (rain, cloud water, cloud ice, snow, and graupel) were used to calculate the radar reflectivity. We use the level-2.5 closure of the Mellor–Yamada–Nakanishi–Niino turbulence scheme to represent subgrid-scale turbulences (Nakanishi and Niino 2004). For shortwave and longwave radiation processes, the Model Simulation Radiation Transfer code (MSTRN) X (Sekiguchi and Nakajima, 2008) is used. See http://r-ccs-climate.riken.jp/scale/ for more detail.

We performed an offline nesting simulation. The horizontal grid spacings and the number of vertical levels for the outer (inner) domain were 15 km (3 km) and 36 levels (56 levels), respectively. Hereafter, the simulation for the outer (inner) domain is referred to as D1 (D2) (Fig. 7a). The initial and lateral boundary conditions for D1 were taken from the National Centers for Environmental Prediction (NCEP) Global Forecasting System (GFS) operational analyses at 0.5° resolution every 6 hour. The initial and lateral boundary conditions for D2 were taken from D1. The simulation covers the period from 0000 UTC 28 July 2015 (0000 UTC 28 July 2015) to 0000 UTC 9 August 2015 (0000 UTC 7

268   August 2015) for D1 (D2).

269   Figure 7 shows the Soudelor's track and minimum sea level pressure (MSLP) at the typhoon center

270   from the best track of the Japan Meteorological Agency (JMA) and the D1 and D2 simulations. The

271   JMA best track shows a rapid decrease of MSLP during the three days from 1 August. D1 captures the

272   rapid intensification while D2 shows a slightly slower intensification than the best track. As for the

273   track, both D1 and D2 closely follow the best track albeit slightly shifted northward. We used D2 as a

274   reference to simulate radar observations.

275

276   **4.2.   Results**

277   Figures 8 and 9 show radar reflectivity near the surface level and its vertical cross section in a mature

278   stage of the simulated Soudelor (0000 UTC 5 August 2015). The results are shown in the longitude-

279   latitude coordinate for Fig. 8 (a) and in the scan-angle coordinate of the GPR for Fig. 8 (b-d) covering

280   the same domain as Fig. 8 (a). As in the homogeneous case, areas where the reflectivity from

281   precipitation exceeds 0 dBZ are shaded by grey.

282   Figure 8 (a) and 9 (a) show the reflectivity of the full-resolution nature run for reference. The figures

283   show the typical structure of a tropical cyclone characterized by no rainfall within the eye, heavy

284   rainfall in the eye wall, and the spiral outer-rainband structure.

285   The bw20bs20 captures the spatial distribution well but without fine structures. The difference is

286   noticeable in the outer rainband (gray-colored area) in which the shape of the bands is different from

287   the reference. With the tilted and relatively large scattering volume, the radar catches the signal of

288   precipitation that is in the level higher than the level shown in the figure. The bw20bs20 also misses

289   the local maxima of precipitation. For instance, the strongest precipitation south of the eye (red area

290   in Fig. 8a) was not well captured by bw20bs20. This is because the echo from sharp and strong

291   precipitation was averaged out due to NUBF within the relatively large scattering volume. For the

292   vertical cross-section, the observation roughly captures the structure albeit in a jaggy and discretized

12

293   manner because of the tilted and relatively large scattering volume (Fig. 9b). The tilted scattering

294   volume also results in the precipitation echo taller than the reference as discussed in Sect. 3.

295   On the other hand, the satellite observes precipitation accurately for both spatial and vertical cross-

296   sections in bw05bs05 (Fig. 8d and Fig. 9d).

297   In the case of bw20bs05 (i.e. oversampling case), the radar inherited the shortcomings in bw20bs20

298   due to the wide beam width: the larger precipitated area in the outer rainband (Fig. 8c) and taller

299   precipitation pattern (Fig. 9c) compared with the reference. On the other hand, the results were

300   arguably improved thanks to the fine sampling span compared with bw20bs20. For instance, the strong

301   precipitation south of the eye was well captured compared with bw20bs20 (Fig. 9c). Furthermore,

302   individual convective cells south of the typhoon were observed as individual cells although they were

303   blurred due to NUBF within the large scattering volume. This is because the finer sampling span

304   increased the probability for the beam center to hit the area of heavy rainfall.

305   To compare the skills quantitatively, we computed the threat scores with a threshold of 20, 30, 40,

306   and 50 dBZ for all the experiments. Figure 10 shows that bw05bs05 is the best and also shows the

307   benefit of oversampling. Namely, the score of bw20bs05 increased by more than 20 % on average for

308   all the thresholds compared with that of bw20bs20.

309   Figures 9 and 10 also shows the impact of the surface clutter. The hatched area in Fig. 9 shows the

310   area where SCR is less than or equal to zero. Assuming that the SCR of zero is the minimum threshold

311   to indicate whether the clutter interference will be serious (Li et al., 2017), the hatched area is

312   considered as unobservable. The unobservable area was confined up to 3-km in bw05bs05, while they

313   reached as high as 7 km in bw20bs20 and bw20bs05. Thus, to reduce the impact of the surface clutter,

314   the beam width needs to be narrow enough.

315

5.   Dependence on the position of typhoon

317   At other than the nadir point, the radar observes precipitation obliquely and consequently the

318   precipitation echo is easy to be contaminated by the surface clutter. As mentioned in Sect. 3, how

319   severely surface clutter contaminates the precipitation echo depends on the incidence angle of the beam,

320   which corresponds to the distance from the nadir. Therefore, the location of the target precipitation

321   system should have an impact on the quality of the observations. This section investigates the

322   sensitivity to the location of the typhoon.

323   We used the simulated Typhoon Soudelor as the reference as in Sect. 4. We picked out the mature

324   stage of the typhoon whose center is in 18° N, 136° E as an example and moved it north and south to

325   represent typhoons whose center is in 10° N, 20° N, and 30° N. We assumed the longitudinal position

326   of the typhoon centers were the same as the sub-satellite point for all the cases to compare the

327   difference originating from the latitudinal position of the typhoon center. The radar used in this section

328   was the same as the one in the bw20bs05.

329   Figure 11 shows the precipitation echo at the near surface level for the three cases together with the

330   reference. Among them, the precipitation pattern in 10° N was the most similar to the reference, and

331   the threat score was the highest (Fig. 13). As the typhoon position is away from the sub-satellite point,

332   the precipitation is observed weaker with the outer-rainband area more expanded, and the threat score

333   becomes lower (Fig. 13). As discussed in the previous sections, those are due to the widely tilted

334   scattering volume with which the beam captures the signal of precipitation in high altitude whose

335   intensity is weaker than that in the level shown (cf. Fig. 12). The tilted scattering volume also resulted

336   in vertically extended precipitation echo (Fig. 12). The further away from the nadir, the more vertically

337   extended the precipitation echo. This is also true for the clutter height ($SCR \leq 0$): the further away

338   from the nadir, the higher the clutter height. However, this is only the case for the area with weak

339   precipitation. In the area with heavy precipitation at a higher latitude, the impact of the surface clutter

340   is limited to the near surface level. For instance, the strongest precipitation in the south of the eye is

341   not affected by the surface clutter at all in the case of 30° N (Fig. 12d), while those are masked by the

342   clutter in the cases of 10° N and 20° N (Fig. 12b and 12c). Those results are also evident in the threat

14

343   score (dashed line in Fig. 13). The surface clutter is determined by cross section σ_0 integrated over

344   the scattering area A, and both σ_0 and A decrease along with the incidence angle in this area.

345   Therefore, the echo from the sea surface clutter becomes smaller and SCR becomes larger along with

346   the latitude.

347   We obtained the similar results as shown in Sect. 3 with the typhoon case. When the observation

348   target is in low latitude (i.e. close to the nadir), the clutter height is low, and the radar can observe weak

349   precipitation free from clutter at high altitudes. It should be difficult to observe precipitation at the near

350   surface level, even if the precipitation is strong. In case the radar observes precipitation in mid-latitudes

351   (i.e. away from the nadir), the radar cannot observe weak precipitation at most of the altitude while it

352   is easier to observe strong precipitation at any altitude.

353

354   **6.   Impact of attenuation and sidelobe clutter**

355   In the previous sections, we did not consider the impact of attenuation and sidelobe clutter, assuming

356   that they can be corrected (e.g. Iguchi et al., 2000) or filtered (e.g. Kubota et al., 2016). In this section,

357   we investigate the impact of attenuation and sidelobe clutter. To consider attenuation, the attenuation

358   coefficient is included in the calculation of P_r, P_s, and Z (Eqs. 3, 6, and 7). The attenuation

359   coefficients are calculated with Eq. (5), and the extinction coefficients are calculated by Joint-

360   Simulator (Hashino et al., 2013). To investigate the impact of sidelobe clutter, the observation volume

361   is expanded to include the sidelobe area up to the fifth null point (Fig. 1).

362   Figure 14 shows the cross-section of the typhoon with various radar parameters; bw20bs20,

363   bw20bs05, and bw05bs05. Due to the attenuation, reflectivity from heavy rain is weakened for all the

364   cases (c.f. the reflectivity at south of the eye). This feature is also evident in the threat score for the

365   case with bw20bw05 (Fig. 15). Figure 15 compares three cases: The first case ("main") does not

366   consider the impact of attenuation, and its observation volume does not include sidelobe area, i.e., the

367   same as the bw20bs05 in Fig. 10. The second case ("main+side") does not consider the impact of

attenuation, but its observation volume includes sidelobe area, i.e., considering the impact of sidelobe clutter. The third case ("main+atten.") considers the impact of attenuation, but its observation volume does not include the sidelobe area. Figure 15 shows that the threat score of "main+atten." is almost identical to that of "main" and the impact of attenuation is negligible with the thresholds of 20, 30, and 40 dBZ. On the other hand, the threat score of "main+atten." with the threshold of 50 dBZ is zero at all heights. Therefore, the attenuation makes it difficult to obtain rain echoes from strong precipitation.

On the other hand, the sidelobe clutter contaminates the weak to moderate rain echoes. For example, the top of convection at around 17°N is masked by the sidelobe clutter for the cases with low resolution beam (Figs. 14a and 14b). Figure 15 also shows that threat scores of "main+side" are smaller than that of "main" for the thresholds of 20, 30, and 40 dBZ while the impact is negligible with the threshold of 50 dBZ. Therefore, the sidelobe clutter contaminates weak to moderate rain.

7.   Summary

We examined the feasibility of radar observation for precipitation from a geostationary satellite. The results demonstrated that it would be possible to obtain three-dimensional precipitation data. However, the quality of the observation was found to depend on the beam width, the beam sampling span, and the position of targeting precipitation systems. With the wide beam width and coarse beam span, the radar cannot observe weak precipitation at low altitudes. The limitations can be somewhat mitigated by oversampling (i.e., a wide beam width but a fine sampling span). With the narrow beam width and fine beam sampling span, the surface clutter interference was confined to the surface level. For the position of the target precipitation system, the larger (smaller) the off-nadir angle, the easier (more difficult) it is to obtain the precipitation signal if the precipitation is strong (weak).

This study also investigated the impact of attenuation and sidelobe clutter. The attenuation hinders to obtain rain echoes from strong precipitation while the sidelobe clutter contaminates signals from weak precipitation. An attenuation correction method like the surface-reference method (e.g. Iguchi et

al., 2000; Meneghini et al., 2000) and a clutter filter (e.g. Kubota et al., 2016) must be devised to mitigate the detrimental impacts. One possible idea for the filter may be to distinguish an echo from precipitation and surface by using Doppler shift, but this remains to be a subject of future research.

If the wide beam width of 0.032° is used, the raw product may be prohibitively coarse for a specific purpose. One possible way to effectively downscale such observations is to assimilate the data for NWP. By doing this, the information can be treated properly, and we can get precipitation information in the prediction model coordinate. However, it is not trivial whether assimilation of such data is useful for NWP. In the future, an observing system simulation experiment (OSSE) will be conducted using precipitation measurements simulated with the simulator developed in this study to evaluate the potential impacts of the GPR on NWP. Given that wind field observation may be possible from a geostationary satellite as shown in Lewis et al. (2011), the combined use of both observations would be an attractive option.

Reference

Bessho, K., Date, K., Hayashi, M., Ikeda, A., Imai, T., Inoue, H., Kumagai, Y., Miyakawa, T., Murata, H., Ohno, T., Okuyama, A., Oyama, R., Sasaki, Y., Shimazu, Y., Shimoji, K., Sumida, Y., Suzuki, M., Taniguchi, H., Tsuchiyama, H., Uesawa, D., Yokota, H., Yoshida, An introduction to Himawari-8/9: Japan's new-generation geostationary meteorological satellites, J. Meteorol. Soc. JPN., 94, 151‑183, 2016.

Bliven, L. F., Sobieski, P. W., and Craeye, C., Rain generated ring-waves: Measurements and modelling for remote sensing, Int. J. Remote. Sens., 18, 221-228, 1997.

Braus, N., Gade, M., and Lange, P. A., Radar backscattering measurements of artificial rain impinging on a water surface at different wind speeds, paper presented at 1999 International Geoscience and Remote Sensing Symposium (IGARSS), Inst. of Elect. and Elect. Eng., New York, 1999.

Cho, H.-K., Bowman, P. B., and North, G. R., Equatorial waves including the Madden-Julian Oscillation in TRMM rainfall and OLR data, J. Climate, 17, 4387-4406, 2004.

Contreras, R. F., Plant, W. J., Keller, W. C., Hayes, K., and Nystuen, J., Effects of rain on Ku-band backscatter from the ocean, J. Geophys. Res., 108, C5,3165, 2003.

Gaspari, G., and Cohn, S., Construction of correlation functions in two and three dimensions, Q. J. Roy. Meteor. Soc., 125, 723-757, 1999.

Hashino, T., Satoh, M., Hagihara, Y., Kubota, T., Matsui, T., Nasuno, T., and Okamoto, H., Evaluating cloud microphysics from NICAM against CloudSat and CALIPSO, J. Geophys. Res. Atmos., 118, 7273-7292, 2013.

Hamada, A., Takayabu, Y. N., Liu, C., and Zipser, E. J., Weak linkage between the heaviest rainfall and tallest storms, Nat. Commun, doi: 10.1038/ncomms7213, 2015.

Hou, A. Y., R. K. Kakar, S. Neeck, A. A. Azarbarzin, C. D. Kummerow, M. Kojima, R. Oki, K. Nakamura, and T. Iguchi, 2014: The global precipitation measurement mission. Bull. Amer. Meteor. Soc., 95, 701-722.

Houze, R. A., Rasmussen, K. L., Zuluaga, M. D., and Brodzik, S. R., The variable nature of convection in the tropics and subtropics: A legacy of 16 years of the Tropical Rainfall Measuring Mission satellite, Rev. Geophys., 53, 994-1021, 2015.

Iguchi, T., Kozu, T., Meneghini, R., Awaka, J., Okamoto, K., Rain-profiling algorithm for the TRMM precipitation radar, J. Appl. Meteorol., 39, 2038-2052, 2000.

Im, E., Smith, E. A., Chandrasekar, V. C., Chen, S., Holland, G., Kakar, R., Tanelli, S., Marks, F., and Tripoli, G., Workshop report on NEXRAD-In-Space -A geostationary satellite doppler weather radar for hurricane studies, 33rd Conf. on Radar Meteorology, Cairns, QLD, Australia, Amer. Meteor. Soc., 4B.5, 2007 [Available online at http://ams.confex.com/ams/pdfpapers/123726.pdf.].

Joudoi, D., Kuratomi, T., and Watanabe, K., The construction method of a 30-m-class large planar antenna for Space Solar Power Systems, 69th International Astronautical Congress, Bremen, Germany, 1-5, October 2018.

Kelley, O. A., Stout, J., and Halverson, J. B., Tall precipitation cells in tropical cyclone eyewalls are

18

associated with tropical cyclone intensification, Geophys. Res. Lett., 31, L24112, 2004.

Kidd, C., Becker, A., Huffman, G. J., Muller, C. L. Joe, P., Skofronick-Jackson, G., and Kirschbaum, D. B., So, how much of the earth's surface is covered by rain gauges?, B. Am. Meteorol, Soc., doi: 10.1175/BAMS-D-14-00283.1, 2016.

Kozu, T, T. Kawanishi, H. Kuroiwa, M. Kojima, K. Oikawa, H. Kumagai, K. Okamoto, M. Okumura, H. Nakatshka, and K. Nishikawa, Development of precipitation radar onboard the Tropical Rainfall Measuring Mission (TRMM) satellite. IEEE Trans. Geosci. Remote Sens., 39, 102-116, 2001.

Kubota, T., Iguchi, T., Kojima, M., Liao, L., Masaki, T., Hanado, H., Meneghini, R., and Oki, R., A statistical method for reducing sidelobe clutter for the Ku-band precipitation radar on board the GPM Core Observatory, J. Atmos. Oceanic Technol., 33, 1413-1428, 2016.

Kummerow, C., W. Barnes, T. Kozu, J. Shiue, and J. Simpson, The Tropical Rainfall Measuring Mission (TRMM) sensor package, J. Atmos. Oceanic Technol., 15, 808–-816, 1998.

Lewis, W. E., Im, E., Tanelli, S., Haddad, Z., Tripoli, G. J., Smith, E. A., Geostationary doppler radar and tropical cyclone surveillance, J. Atmos. Ocean. Tech., 28, 1185-1191, 2011.

Li, X., He, J., Wang, C., Tang, S., Hou, X., Evaluation of surface clutter for future geostationary spaceborne weather radar, Atmosphere, 8, 14, doi: 10.3390/atmos8010014, 2017.

Kubota, T., Shige, S., Hashizume, H., Aonashi, K., Takahashi, N., Seto, S., Hirose, M., Takayabu, Y. N., Ushio, T., Nakagawa, K., Iwanami, K., Kachi, M., Okamoto, K., Global precipitation map using satellige-borne microwave radiometers by the GSMaP Project: Production and validation, IEEE T. Geosci. Remote., 45, 7, 2259-2275, 2007.

Masunaga, H., and Kummerow, C., Combined radar and radiometer analysis of precipitation profiles for a parametric retrieval algorithm, J. Atmos. Ocean. Tech., 22, 909-929, 2005.

Meguro, A., Shintate, K., Usui, M., and Tsujihata, A., In-orbit deployment characteristics of large deployable antenna reflector onboard Engineering Test Satellite VIII, Acta Astronautica, 65(9-10), 1306-1316, 2009.

Meneghini, R., Iguchi, T., Kozu, T., Liao, L., Okamoto. K., Jones, J. A., and Kwiatkowski, J., Use of the surface reference technique for path attenuation estimates from the TRMM radar, J. Appl. Meteorol., 39, 2053-2070, 2000.

Morita, J., Takayabu, Y. N., Shige, S., Kodama, Y., Analysis of rainfall characteristics of the Madden-Julian oscillation using TRMM satellite data, Dynam. Atmos. Oceans, 42, 207-126, 2006.

Nakanishi, M., and Niino, H., An improved Mellor–Yamada level-3 model with condensation physics: Its design and verification, Bound.-Lay. Meteorol., 112, 1–31, 2004.

Okamoto, K., Aonashi, K., Kubota, T., Tashima, T., Experimental assimilation of the GPC Core Observatory DPR reflectivity profiles for Typhoon Halong (2014), Mon. Weather Rev., 144, 2307-2326, 2016.

Otsuka, S., Kotsuki, S., Miyoshi, T., Nowcasting with data assimilation: A case of global satellite mapping of precipitation, Weather Forecast., 31, 1409-1416, 2016.

489 Sekiguchi, M., and Nakajima, T., A k-distribution-based radiation code and its computational
490 optimization for an atmospheric general circulation model, J. Quant. Spectrosc. Ra.,J. Quant.
491 Spectrosc. Radiat. Transfer, 109, 2779–2793, 2008.
492 Skofronick-Jackson, G., Petersen, W. A., Berg, W., Kidd, C., Stocker, E. F., Kirschbaum, D. B., Kakar,
493 R., Braun, S. A., Huffman, G. J., Iguchi, T., Kirstetter, P. E., Kummerow, C., Meneghini, R., Oki,
494 R., Olson, W. S., Takayabu, Y., Furukawa, K., Wilheit, T., The global precipitation measurement
495 (GPM) mission for science and society, B. Am. Meteorol. Soc., 98, 1679-1695, 2017.
496 Takahashi, N., Surface echo characteristics derived from the wide swath experiment of the
497 precipitation radar onboard TRMM satellite during its end-of-mission operation, IEEE T. Geosci.
498 Remote., 55, 4, 1988-1993, 2017.
499 Takayabu, Y. N., Rain-yield per flash calculated from TRMM PR and LIS data and its relationship to
500 the contribution of tall convective rain, Geophys. Res. Lett., 33, L18705, 2006.
501 Tomita, H., New microphysical schemes with five and six categories by diagnostic generation of cloud
502 ice, J. Meteorol. Soc. JPN., 86A, 121-142, 2008.
503 Wentz, F. J., Peteherych, S., Thomas, L. A., A model function for ocean radar cross sections at 14.6
504 GHz, J. Geophys. Res., 89, c3, 3689-3704, 1984.
505

506 **Tables**

507

508 **Table 1** Specifications of the precipitation radar aboard geostationary satellite

Parameter	Value
Frequency	13.6GHz
Scan angle	±6°
Range resolution	≤500m
Horizontal resolution	20km at nadir
Observation range	30km at nadir

509

510 **Table 2** Radar settings. The figures show the resolution at the nadir point.

Experiment	Beam width	Beam span
bw05bs05	5km	5km
bw20bs05	20km	5km
bw20bs20	20km	20km

511

512

513   **Figures**

514

515
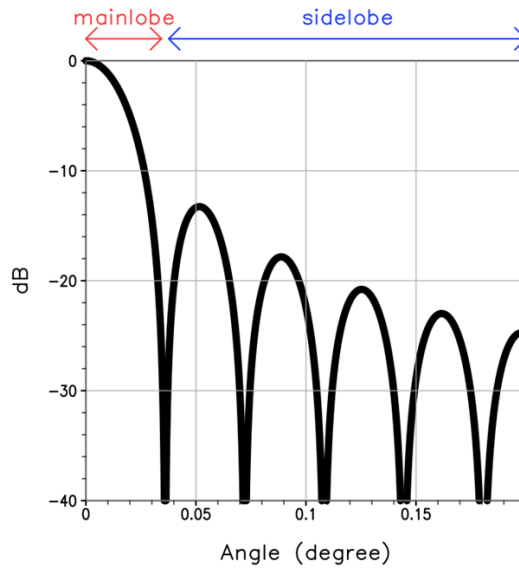
Figure 1 Beam pattern (dB) as a function of beam direction angle (degree).

517

518
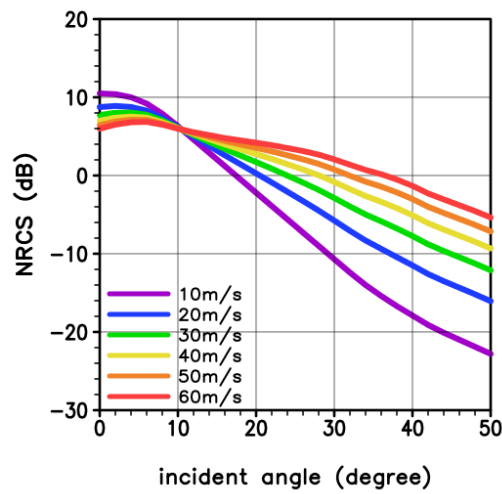
Figure 2 Normalized radar cross section (dB) as a function of incidence angle for six cases of 10-m

520   wind speed.

521
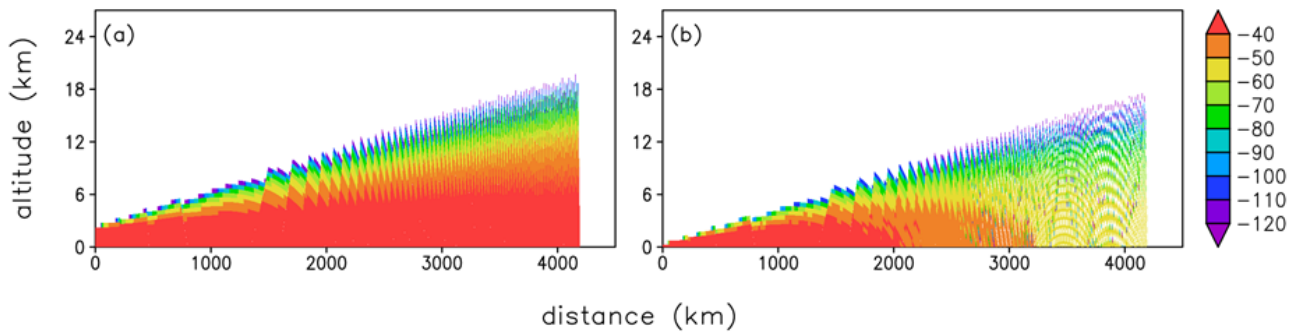
Figure 3 Received power from (a) precipitation, and (b) sea surface clutter, normalized by P_t (dB).
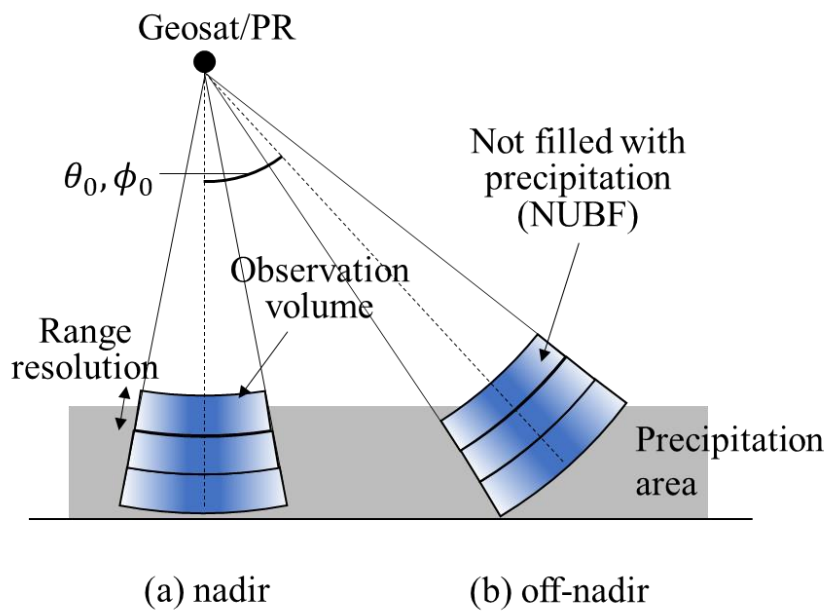
Figure 4 Schematic image of the scattering volume at (a) nadir, and (b) off-nadir.

528
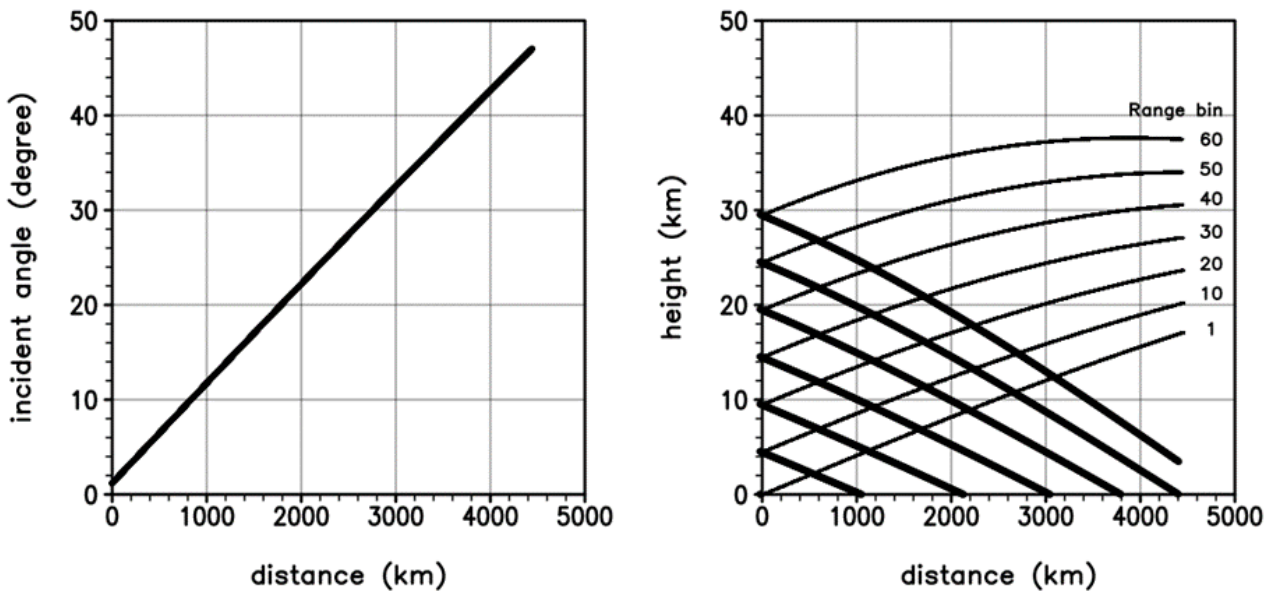
Figure 5 Incidence angle (a) and height of the radar scattering volume (b) as a function of the distance

from the nadir. Thick and thin lines in (b) shows the lower and upper bound, respectively.

531

532
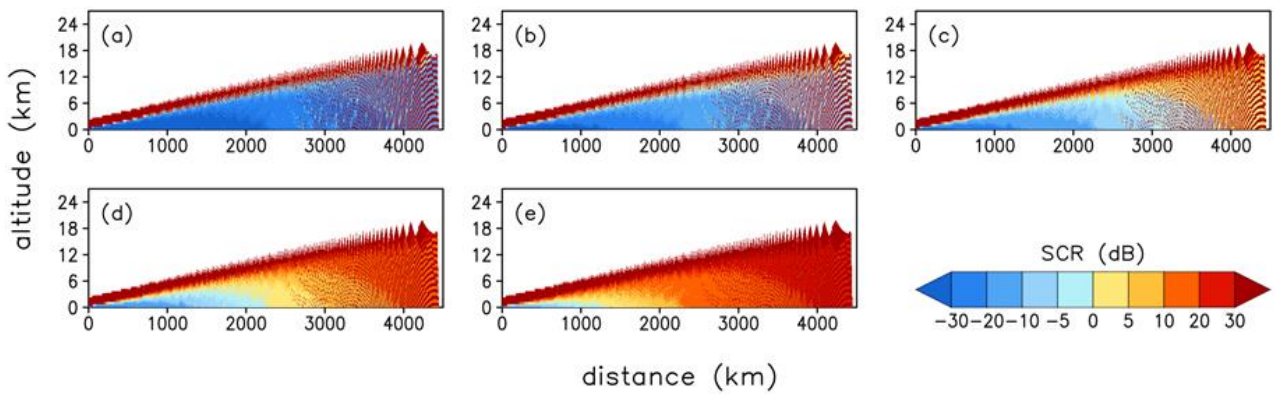
Figure 6 Signal-to-clutter ratio (SCR) in measuring five precipitation intensity (a) 20, (b) 30, (c) 40,

(d) 50, and (e) 60 dBZ as a function of the distance from the nadir (km). It is assumed that the altitude

lower than 2 km is filled with homogeneous precipitation.

536

24
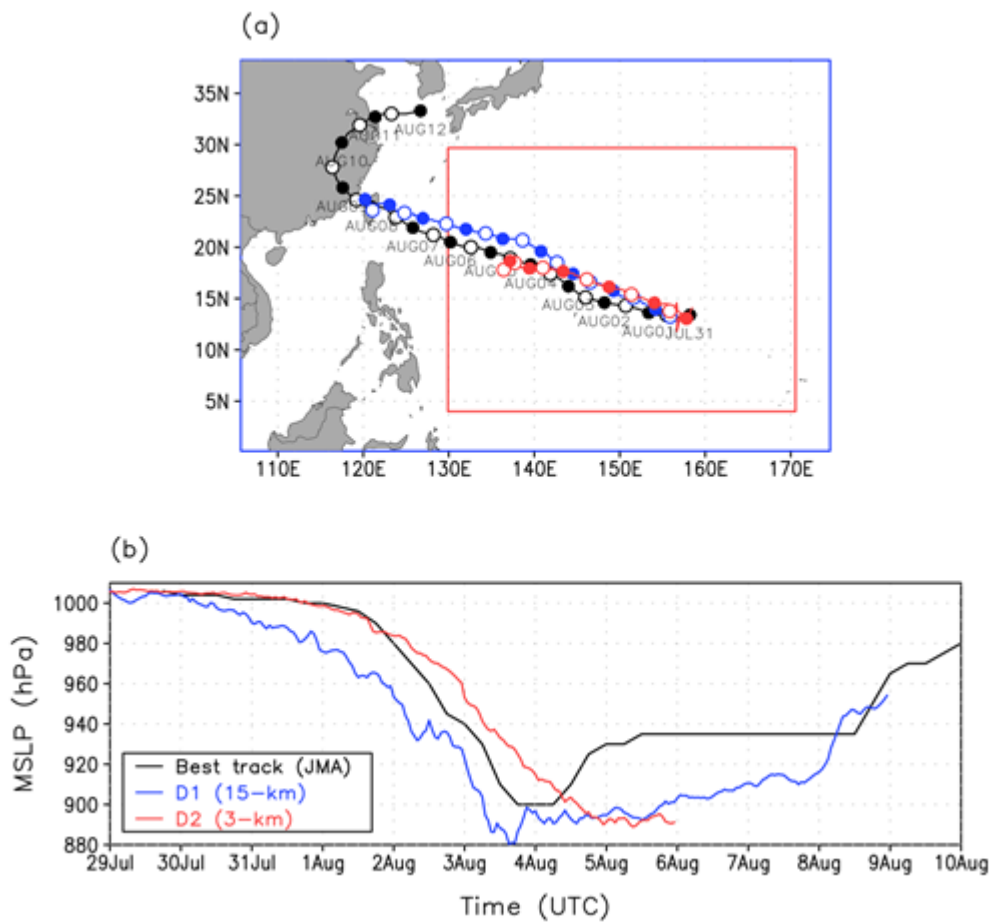
Figure 7 (a) Model domains for D1 (blue) and D2 (red) and typhoon tracks, and (b) time series of minimum sea level pressure (MSLP). Black, blue, and red colors show the JMA best track data, D1 simulation, and D2 simulation, respectively. Closed and open circles in (a) denote the typhoon positions at 0000 UTC and 1200 UTC, respectively.

543
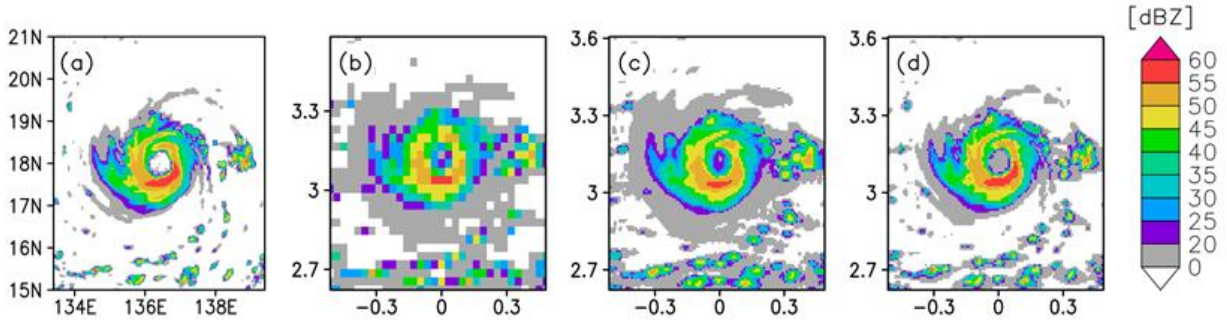
Figure 8 Radar reflectivity (dBZ) near the surface in the typhoon mature stage (0000 UTC, 5 August

2015) for (a) the truth, (b) bw20bs20, (c) bw20bs05, and (d) bw05bs05. 10-m wind speed is overlaid

in (a). The area where reflectivity from precipitation less than 0 dBZ are left blank.

547
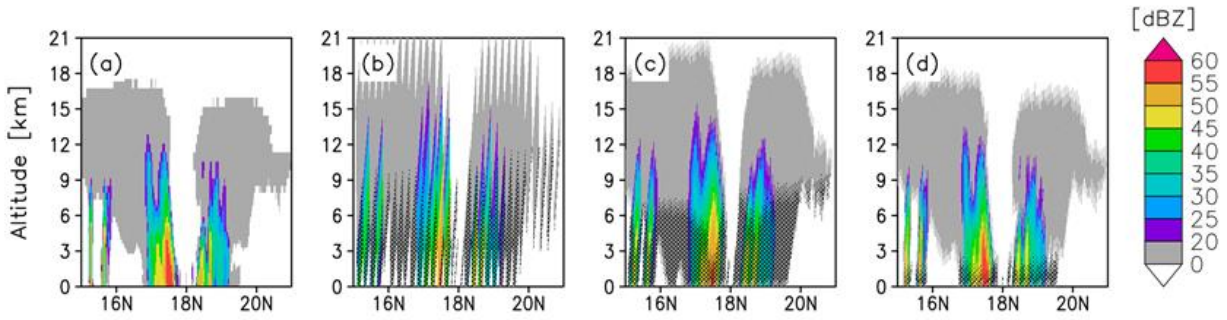
Figure 9 Precipitation reflectivity (dBZ) along 136.4°E longitude line passing through the typhoon

center in the mature stage (0000 UTC, 5 August 2015) for (a) the truth, (b) bw20bs20, (c) bw20bs05,

and (d) bw05bs05. The area where reflectivity from precipitation less than 0 dBZ are left blank and

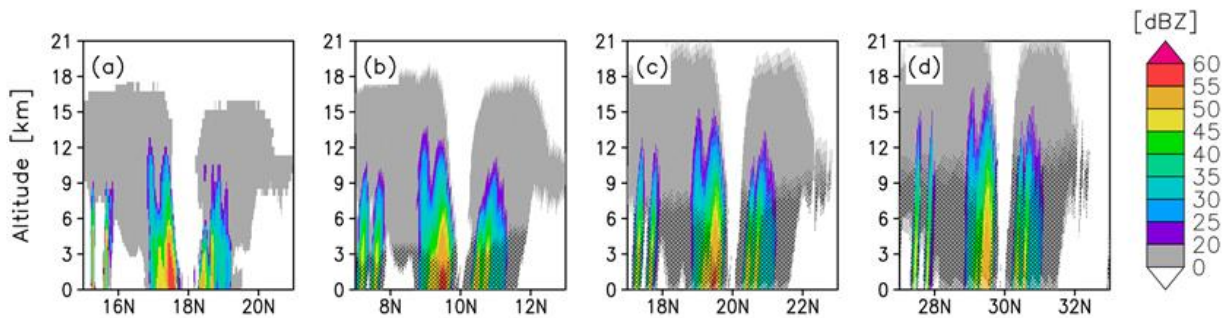the area in which SCR < 0 is hatched in (b-d).

552
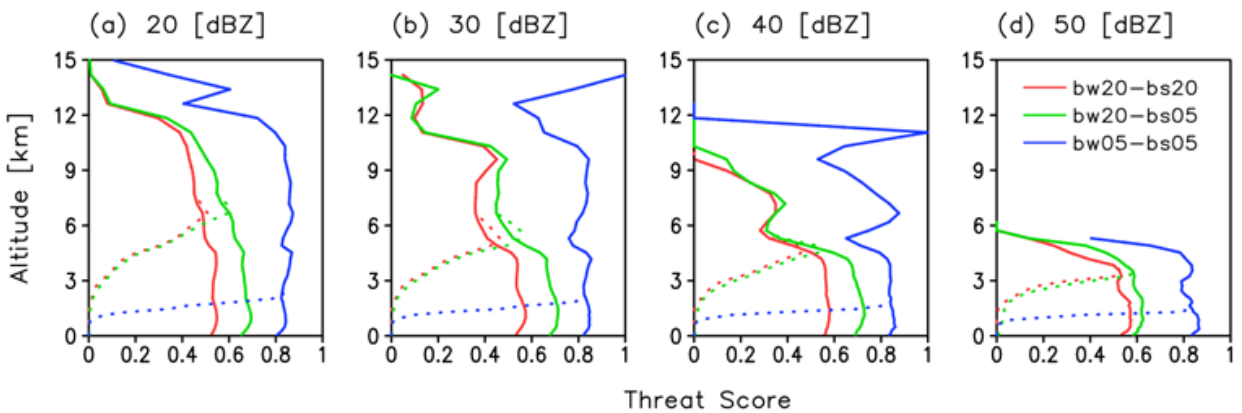
Figure 10 Threat score with a threshold of (a) 20, (b) 30, (c) 40, and (d) 50 (dBZ) for bw20bs20 (red),

554 bw20bs05 (green), and bw05bs05 (blue). The dotted and solid lines show the threat score with and

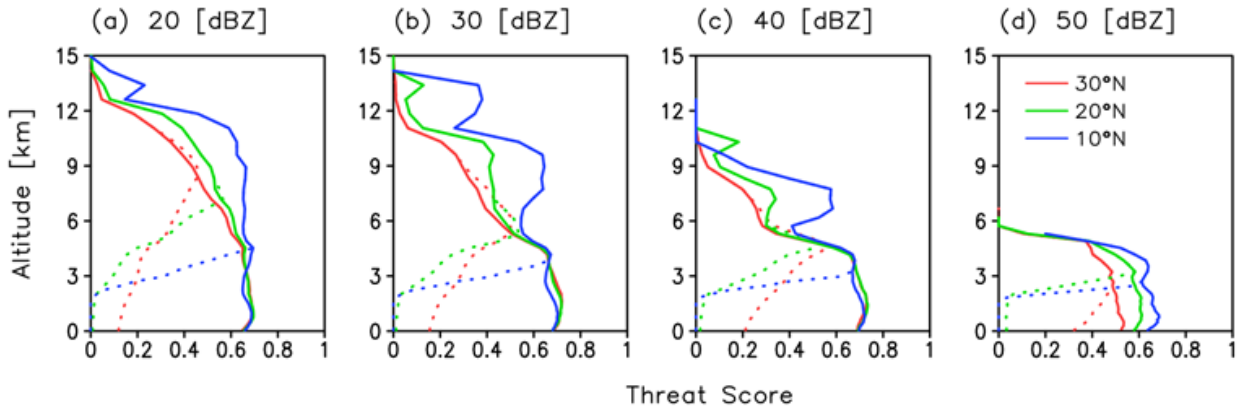555 without considering the impact of surface clutter, respectively.
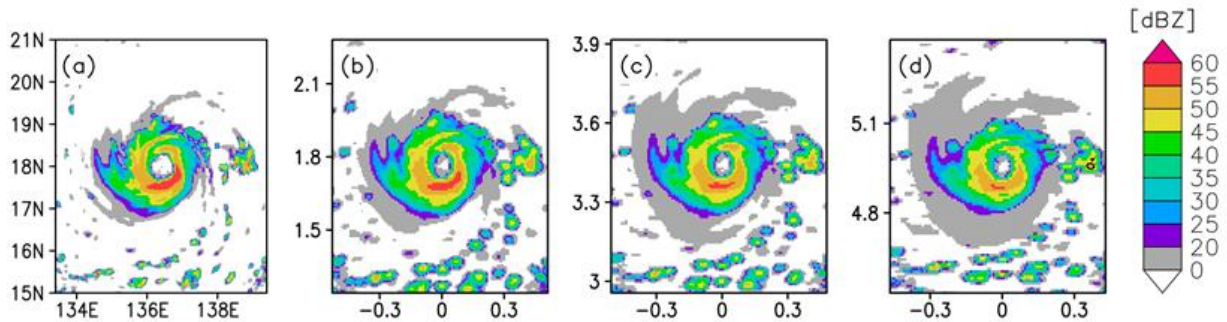
556

557 **Figure 11** Precipitation reflectivity (dBZ) measured with bw20bs05 for the typhoons whose center is

558 in (b) 10°N, (c) 20°N, and (d) 30°N. Contour in (b-d) corresponds to the area SCR > 0. Panel (a) shows

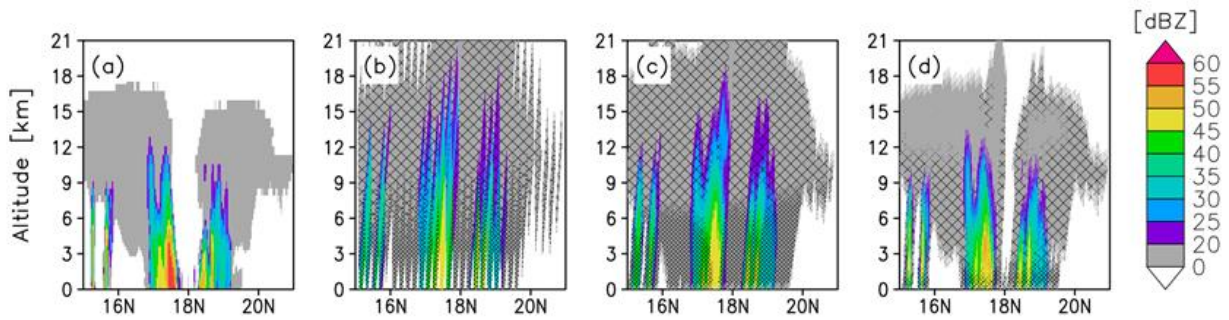559 the truth. The area where reflectivity from precipitation less than 0 dBZ are left blank.

560

561 **Figure 12** Precipitation reflectivity (dBZ) along 136.4°E longitude line passing through the typhoon

562 center measured with bw20bs05 for the typhoons whose center is in (b) 10°N, (c) 20°N, and (d) 30°N.

563 Panel (a) shows the truth. The area where reflectivity from precipitation less than 0 dBZ are left blank

564 and the area in which SCR < 0 is hatched in (b-d).

Figure 13 Threat score with a threshold of (a) 20, (b) 30, (c) 40, and (d) 50 (dBZ) for the typhoons whose centers are at 30°N (red), 20°N (green), and 10°N (blue). The dotted and solid lines show the threat score with and without considering the impact of surface clutter, respectively.


Figure 14 Precipitation reflectivity (dBZ) along 136.4°E longitude line passing through the typhoon center in the mature stage (0000 UTC, 5 August 2015) for (a) the truth, (b) bw20bs20, (c) bw20bs05, and (d) bw05bs05. The area where reflectivity from precipitation less than 0 dBZ are left blank and the area affected (SCR<0) by main lobe (sidelobe) clutter is densely (sparsely) hatched in (b-d).
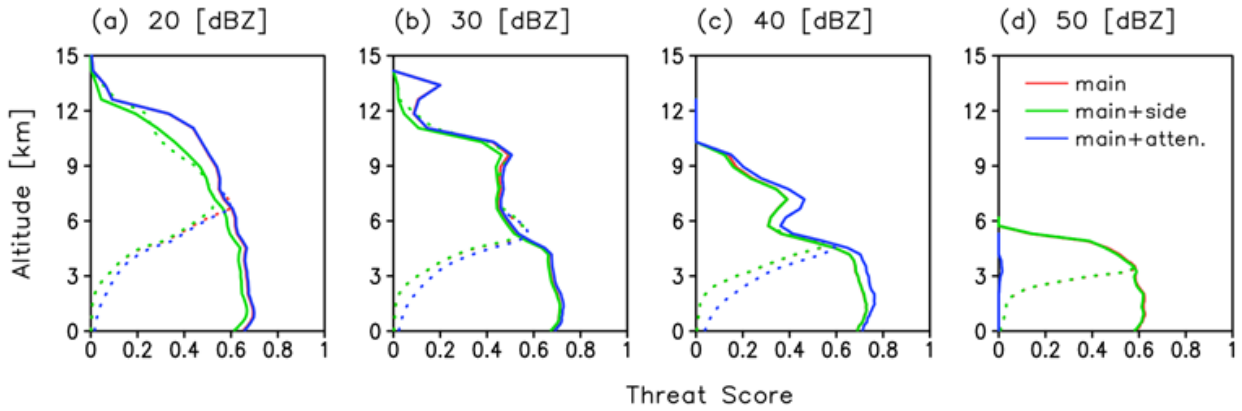
Figure 15 Threat scores with thresholds of (a) 20, (b) 30, (c) 40, and (d) 50 (dBZ) for bw20bs05. Red line overlaps blue line for (a), (b), and (c) and green line for (d). The dotted and solid lines show the threat score with and without considering the impact of surface clutter, respectively.